Electronic Supplementary Material (ESI) for Journal of Materials Chemistry A.

# Direct assessment of structural order and evidence for stacking faults in layered hybrid perovskite films from X-ray scattering measurements

Wen Liang Tan,[a] Yi-Bing Cheng,[ab] and Christopher R. McNeill[a]*

[a] Department of Materials Science and Engineering, Monash University, Wellington Road, Clayton, Victoria 3800, Australia

[b] State Key Laboratory of Advanced Technology for Materials Synthesis and Processing, Wuhan University of Technology, Wuhan, 430070, China

Corresponding Author:

* E-mail: christopher.mcneill@monash.edu

## Electronic Supplementary Information

### S1: Experimental Section

*Chemicals*: Unless stated otherwise, all chemicals were purchased from either Alfa Aesar or Sigma-Aldrich and used as received. Methylammonium iodide (MAI) was purchased from Greatcell Solar Ltd. Butylammonium iodide (BAI) was synthesized according to a previous study.[1]

*Perovskite thin film preparation*: The perovskite precursor solution was prepared by mixing BAI, MAI and $PbI_2$ in the molar ratio of 2:3:4 dissolved in anhydrous *N*,*N*-dimethylformamide (DMF) with 0.3 M $Pb^{2+}$ concentration, targeting $n = 4$ layered perovskite phase. The substrates were cleaned sequentially using the 2 vol% Hellamax solution, deionised water, ethanol and isopropanol, for 15 minutes for each cleaning step, and finally exposed to ozone plasma treatment for 10 minutes prior to film deposition. The perovskite film was deposited using the drop-casting method in ambient atmosphere (relative humidity ~ 40 ± 10 %).[2] The substrate was preheated on a hot plate at 60 °C, followed by dripping 6 μL of the precursor solution at the substrate centre. The precursor solution spread across the substrate circularly, followed by crystallization into the perovskite as the DMF solvent evaporates as indicated by the transformation of yellow precursor solution into the mirror-like black film. The film was further annealed at 100 °C for 2 minutes to completely evaporate the DMF solvent.

*Materials characterization*: The samples were prepared onto the fluorine tin oxide (FTO) coated glass substrate. Scanning electron microscope (SEM) images of perovskite films were recorded on a FEI Magellen 400 FEG microscope using an accelerating voltage of 5 kV. The X-ray diffraction (XRD) patterns of perovskite films were collected with a Bruker D8 Advanced diffractometer (Bragg-Brentano geometry) equipped with a Cu *Kα* X-ray tube operated at 40 kV and 40 mA using a step size of 0.01° and time per step of 0.1 s. UV-vis spectra of perovskite films were recorded using a Perkin Elmer Lambda 950 UV/VIS/NIR spectrophotometer.

*Synchrotron X-ray scattering measurement sample preparation*: The bare silicon substrate was used for GTWAXS measurement. For TWAXS measurement, flexible Mylar film was used as the X-ray transparent substrate. Rather than using the solvent cleaning method, the Mylar film was cleaned by simply blowing the surface vigorously with compressed air. The Mylar film was then placed on a glass substrate and secured using tape to ensure smooth surface, followed by UV ozone treatment for 15 minutes. The perovskite films for both GTWAXS and TWAXS measurement were deposited on the respective substrates using the drop-casting method. A photograph of the perovskite film drop-casted on the Mylar substrate is shown in inset in Figure S2a. The corresponding X-ray diffractogram showed similar film texture as the drop-casted film on the rigid glass substrate (Figure S2a).

*Synchrotron X-ray scattering measurement methods*: The X-ray scattering experiments were performed at the SAXS/WAXS beamline at the Australian Synchrotron. The beam energy was fixed at 12 keV, and focused to the size of 250 μm in width and 28 μm in height. The total exposure time for each scattering pattern is 3 s, with a new spot used for each exposure to minimise X-ray induced damage. The scattering pattern was recorded using a Pilatus 2M detector placed at ~ 67 cm away from the sample, calibrated using the standard sample of silver behenate (AgBeh). The entire beam path from the X-ray source to the detector were placed under vacuum to minimise diffuse scattering from air and enhance signal-to-noise ratio of the scattering pattern. For the GTWAXS experiments, the drop-cast film was cut to remove the rim region to avoid the adventitious X-ray scattering from the microstructure at the rim. The sample was positioned at 0.4° incident angle to the X-ray beam, thereby having *ca.* 4 mm beam footprint in the beam direction. The width of the sample was cut to be less than the beam footprint such that the beam lands the sample edge closer to the detector. The in-plane scattered X-rays from the sample edge experiences minimal attenuation caused by absorption and are hence transmitted through the sample and recorded on the detector. To probe film microstructure at different depth from the surface, the GTWAXS patterns were collected at varying X-ray incident angles of 0.10, 0.125, 0.15, 0.175, 0.20, 0.25, 0.30, 0.40°. For the TWAXS experiments, the sample was placed perpendicular to the X-ray beam. Any anisotropic scattering pattern signifies the misalignment of the sample, which can be adjusted by rotating the sample about the vertical and horizontal axis perpendicular to the X-ray beam.[3] Multiple X-ray scattering patterns were collected for a sample at various locations to ensure reproducibility. The data reduction of 2D scattering patterns was done using Igor Pro with an altered version of NIKA analysis package.[4]

## S2: GIWAXS pattern simulation

The GIWAXS patterns were calculated based on the previously determined single-crystal structures,[5-7] following the method reported by Smilgies *et al*.[8] The program VESTA was used to extract all possible Bragg reflections, and the corresponding theoretical intensities.[9] In the powder diffraction, symmetry-equivalent reflections with the same *d* spacing are superimposed at a single Bragg angle. On the other hand, these reflections can be measured individually with single-crystal diffraction. The GIWAXS measurement on a textured sample with isotropic orientation in-plane discerns symmetry-equivalent reflections, where reflections with different orientation with respect to the crystallographic orientation normal to the substrate are observed as different spots in the GIWAXS pattern. This results in more than one peak with exact same $q$-spacing for a Bragg reflection. Therefore, the intensity of the each GIWAXS peak is the factor of the total intensity for the associated Bragg reflection, depending on the fraction of symmetry-equivalent reflections that lies at that peak position. We present an example using the tetragonal phase of methylammonium lead iodide ($MAPbI_3$) perovskite as shown in Figure S7. The (110) Bragg reflection consists of four symmetry-equivalent reflections, which are 1 1 0, -1 -1 0, -1 1 0 and 1 -1 0 reflections (Figure S7a). In the simulated GIWAXS pattern for textured $MAPbI_3$ with the preferred [110] out-of-plane orientation, the 1 1 0 reflection is observed in the out-of-plane direction (along $q_{xy}$ = 0 Å$^{-1}$) at $q_z$ = 1 Å$^{-1}$ (Figure S7b). The -1 -1 0 reflection is mirrored about the $q_{xy}$-axis at $q_z$ = -1 Å$^{-1}$, however not observed in the grazing incidence geometry. The remaining -1 1 0 and 1 -1 0 reflections are observed in the in-plane direction (along $q_z$ = 0 Å$^{-1}$) at $q_{xy}$ = ±1 Å$^{-1}$. As the GIWAXS pattern is symmetric about the $q_z$- and $q_{xy}$-axis, the intensity of (110) Bragg reflections in both out-of-plane and in-plane directions which depends on the fraction of total symmetry-equivalent reflections are 50%. The simulated intensities for each GIWAXS peak are represented by the bubble size and colour in the simulated GIWAXS patterns, expressed in the logarithmic scale as shown in Figure S5.

## S3: Williamson-Hall analysis

The broadening of diffraction peak is the convolution of instrumental and sample-related broadening. The sources of instrumental broadening in the synchrotron-based X-ray scattering experiment include but not limited to beam energy resolution (ΔE/E), sample-to-detector distance and spatial resolution of the detector, which present regardless of grazing-incidence or transmission geometry. The instrumental broadening contribution due to energy resolution can be neglected as the beamline has the energy resolution of $2 \times 10^{-4}$.[10] Therefore, the minimum instrumental broadening is calculated as about 0.0016 Å$^{-1}$, determined from the $q$-resolution limit ($q = 4\pi \sin\theta/\lambda$ where $2\theta$ = scattering angle, $\lambda$ = wavelength of the X-ray) achievable with our experimental setup employing beam energy of 12 keV, sample-to-detector distance of ~ 670 mm and detector pixel size of 172 µm. The accurate quantification of instrumental broadening which changes as a function of scattering angle can be done by collecting the X-ray diffraction pattern of standard reference materials such as NIST 660b LaB6 standard reference. While the grazing-incidence geometry can cause additional instrumental broadening due to a distribution of sample-to-detector distances associated with the length of the beam footprint on the sample, the TWAXS experiments avoid such instrumental broadening. By comparing the fitted peak width of the silver behenate (AgBeh) calibrant and experimental data (replotted from Figure 3a) measured in transmission geometry as shown in Figure S8, it is evident that the experimental data exhibit at least two times larger peak width than AgBeh. Note that the observed peak broadening in AgBeh profile constitutes of both sample-related broadening and instrumental broadening.[11] Therefore, the much broader peaks in the experimental data attests that the peak broadening in the experimental data are mostly contributed by the sample-related broadening and the instrumental broadening contribution is insignificant. As a result, comparing the peak width in the W-H analysis without deconvoluting the instrumental broadening is qualitatively accurate.

On the other hand, the sample-related broadening includes size ($\beta_{\text{size}}$) and strain ($\beta_{\text{strain}}$) broadening. The strain is related to the local deviation of *d*-spacing due to crystal imperfection, therefore $\beta_{\text{strain}}$ is the $d^*$-dependent broadening. On the other hand, the crystallite size does not depend on the *d*-spacing, therefore $\beta_{\text{size}}$ is the $d^*$-independent broadening. Both $\beta_{\text{size}}$ and $\beta_{\text{strain}}$ have different dependence on the Bragg angle as below:

$$D = \frac{K\lambda}{\beta_{size}\cos\theta} \tag{1}$$

$$\varepsilon = \frac{\beta_{strain}}{4\ \tan\theta} \tag{2}$$

in which $D$ is the mean crystallite size, $K$ is the shape factor, $\lambda$ is the X-ray wavelength, $\varepsilon$ is the microstrain and $\theta$ is the Bragg angle expressed in radian.

By only summing the sample-related broadening and rearranging equation (1) and (2), we obtain:

$$\beta = \beta_{size} + \beta_{strain} = \frac{K\lambda}{D\cos\theta} + 4\varepsilon\tan\theta \tag{3}$$

Further rearrangement of equation (3) gives:

$$\frac{\beta\cos\theta}{\lambda} = \frac{K}{D} + 2\varepsilon\left(\frac{2\sin\theta}{\lambda}\right) \tag{4}$$

$$\beta^* = \frac{K}{D} + 2\varepsilon d^* \tag{5}$$

where $\beta^* = \beta cos\theta/\lambda$ is the peak broadening expressed in reciprocal space unit and $d^* = 2sin\theta/\lambda$ is the diffraction vector. By plotting Williamson-Hall (W-H) analysis which plots $\beta^*$ as a function of $d^*$ following equation (5), the intercept and the slope of the plot indicate size broadening and strain broadening, respectively.[12]

For materials with stacking fault defects, the faulting planes bound the size of the coherently diffracting domain. Therefore, the size broadening is contributed by both crystallite size effect and stacking fault defect. However, stacking fault defects cause only selective broadening of the peaks correspond to the crystal planes parallel to the faulting plane, while the broadening of other peaks is not significant. This results in peak broadening anisotropy, which is reflected in the W-H plot in $n = 3$ phase (Figure 3c) that shows strong scatter of data, and cannot be fitted well with a single linear line.[13-15] The effect of stacking fault defects on size broadening can be discerned by plotting the W-H plot based on the similar group of reflections (i.e. (0*k*0) and (-1*k*1) reflections). The $\beta^*$ line for the group of reflections affected by stacking fault shows a higher intercept than the $\beta^*$ line for the group of reflections unaffected by stacking fault, indicating a more pronounced size broadening due to stacking fault defect.[13-15] Such method had been used to assess the extent of stacking fault defects in the layered perovskites and showed a higher intercept for the group of reflections affected by the stacking fault.[13, 16]

## S4: Supplementary results

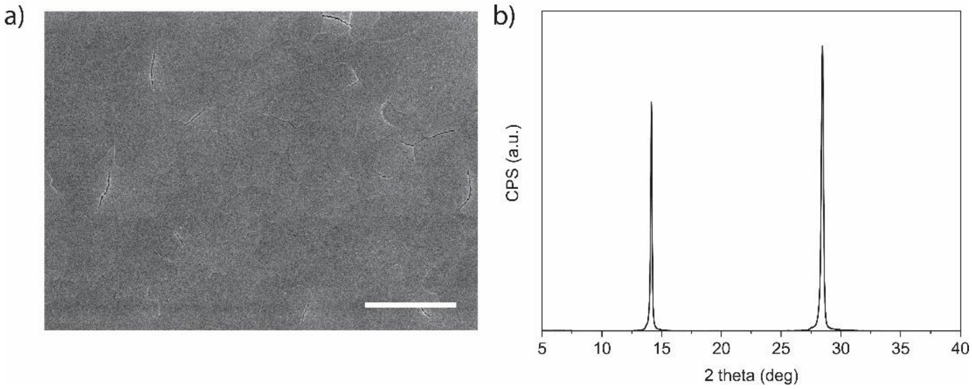

**Figure S1**: Microstructural characterisation of layered perovskite film: (**a**) SEM image of perovskite film shows a smooth surface and pin-hole free morphology, scale bar: 1 µm and the corresponding (**b**) XRD pattern show very intense diffraction peaks at 2θ ~ 14 and 28° only, where diffraction peak at ~ 28° Bragg angle has higher intensity than diffraction peak at ~ 14° Bragg angle, suggestive of highly textured layered perovskite phase. Perovskite films were deposited on FTO substrate.

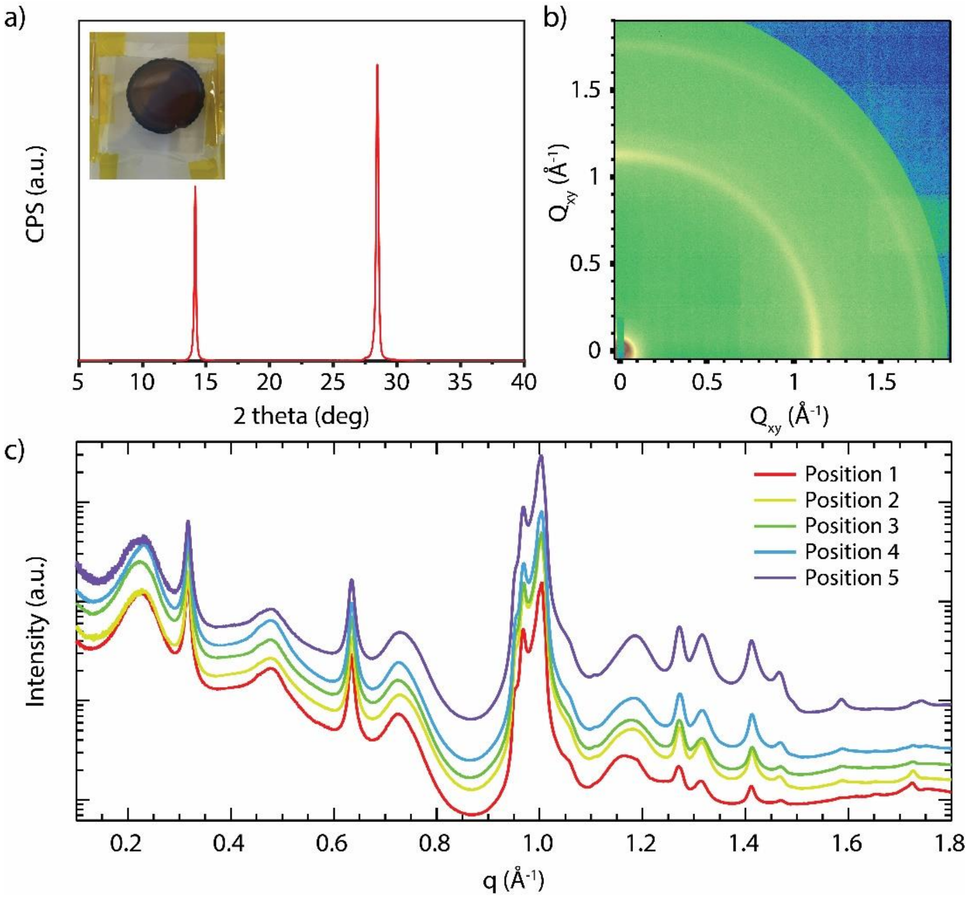

**Figure S2**: (**a**) XRD pattern of perovskite film drop-casted on the flexible Mylar substrate (photograph shown in inset) shows similar XRD pattern as the perovskite film drop-casted on the rigid glass substrate (Figure S1b) confirming similar film microstructure, (**b**) 2D TWAXS pattern of empty Mylar substrate shows very weak isotropic scattering rings at *q* ~ 1.15, 1.25 and 1.75 Å$^{-1}$and (**c**) the radially integrated intensities of the TWAXS pattern collected at various positions in the sample confirms the reproducibility of the TWAXS measurement of perovskite film.

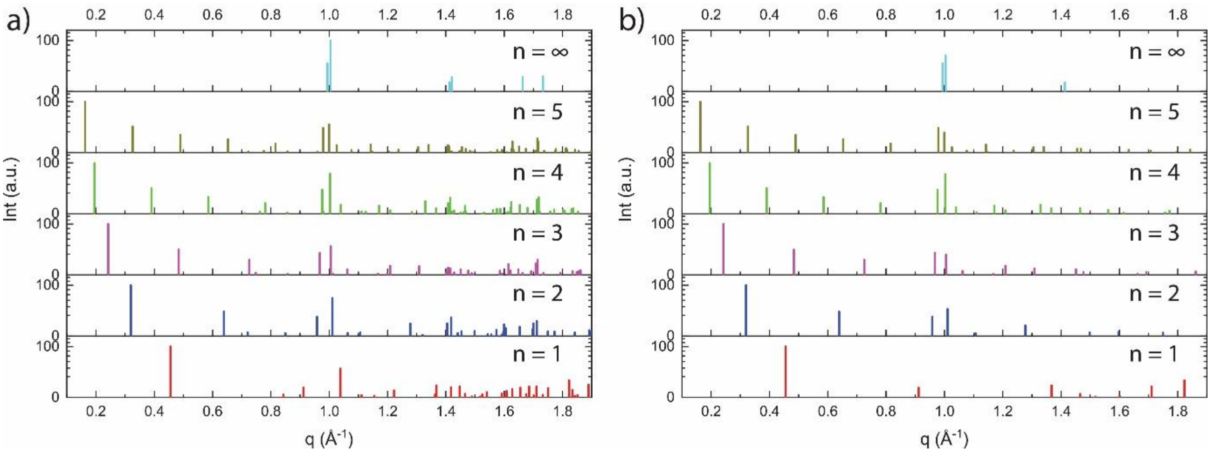

**Figure S3**: Simulation of (**a**) powder XRD peaks for randomly oriented films and (**b**) in-plane XRD peaks for vertically oriented perovskite-like slab for low-*n* phases and [110] out-of-plane oriented for *n*

= ∞ phases based on the previously reported crystal structures.[5-7, 17] The powder XRD peaks were calculated using VESTA.[9] The in-plane XRD peaks is extracted by plotting the simulated GIWAXS pattern of [110] out-of-plane oriented $MAPbI_3$ and [101] out-of-plane oriented layered perovskites in Figure S5 along $q_z = 0$ Å$^{-1}$.

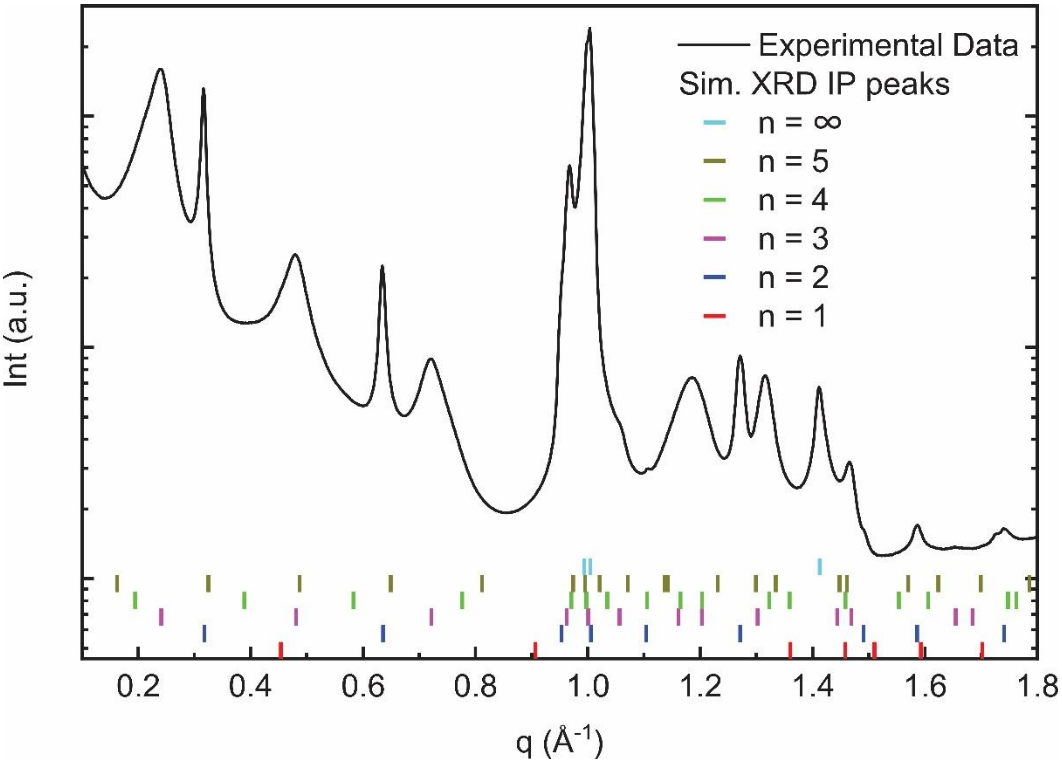

**Figure S4**: Comparison of experimental TWAXS radially integrated intensity with the simulated in-plane diffraction peaks of textured perovskite films of $n$ = 1, 2, 3, 4, 5 and ∞ phases extracted from Figure S5. Due to the similarity of the corner sharing octahedra in the perovskite-like slab for low-$n$ phases with the $n = \infty$ phase, the simulated in-plane diffraction peaks show heavy overlapping above $q$ = 1 Å$^{-1}$. Therefore, the non-overlapping strong diffraction peaks below $q$ = 1 Å$^{-1}$ serve as the guide to differentiate $n$-phases.

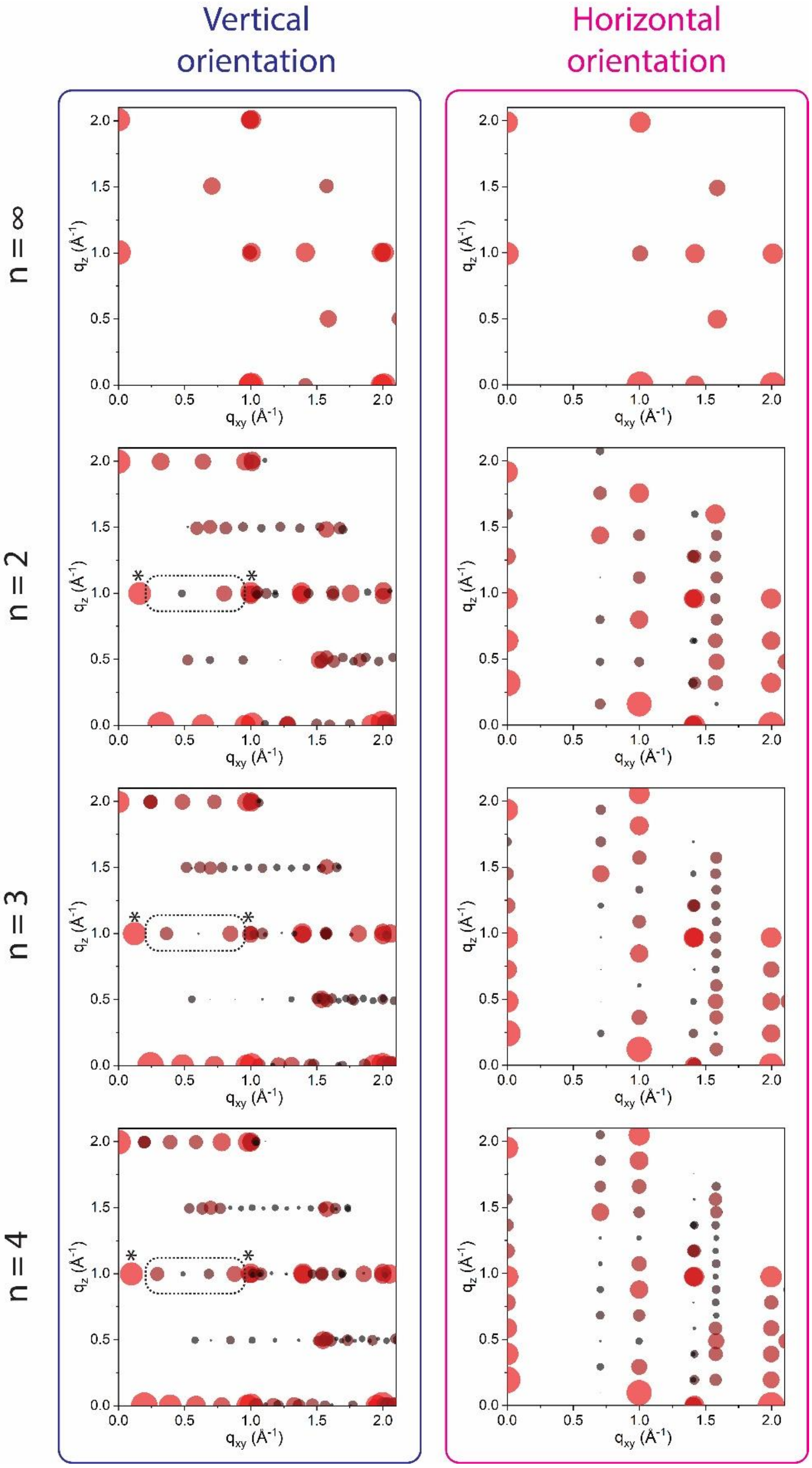

**Figure S5**: Simulated GIWAXS patterns of layered perovskite phases for *n* = 2, 3 ,4 and ∞ for two orthogonal orientations following the methods described in Supplementary Information section S2. The vertical orientation refers to the [110] out-of-plane orientation of *n* = ∞ phase and vertical orientation of perovskite-like slabs for low-*n* phases. The horizontal orientation refers to the [001] out-of-plane orientation of *n* = ∞ phase and horizontal orientation of perovskite-like slabs for low-*n* phases. The appearance of additional spots on top of the spots overlap with the *n* = ∞ phase indicates the formation of layered perovskite phase. The orientation of perovskite-like slabs is discerned by examining the arrangement of these additional spots, where the spots lying along the fixed $q_z$ ($q_{xy}$) value attest the vertical (horizontal) orientation of perovskite-like slabs of the layered perovskite phase. In the case of 'vertical orientation' which is applicable for photovoltaic devices, the *n*-phase of layered perovskite phase can be differentiated from the GIWAXS pattern from the scattering spots along $q_z$ = 1 Å$^{-1}$, between $q_{xy}$ = 0 and 1 Å$^{-1}$. This region is strategically chosen due to least peak overlapping of different *n*-phases, and the number of evenly spaced spots (indicated by the black dotted boxes) resides between those spots overlap with *n* = ∞ phase (marked *) coincides with the integer '*n*'.

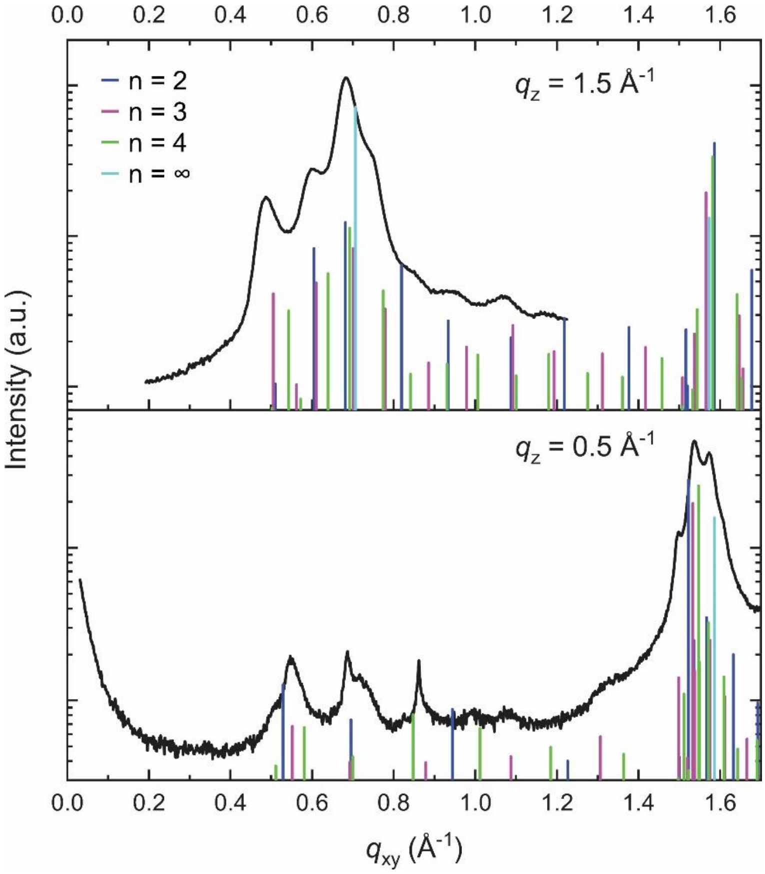

**Figure S6**: Comparison of horizontally integrated line profiles of 2D GTWAXS pattern along $q_z$ = 0.5 and 1.5 Å$^{-1}$ with the simulated patterns in Figure S5. The experimental peaks match well with *n* = 3 phase despite heavy peak overlapping from different *n*-phases.

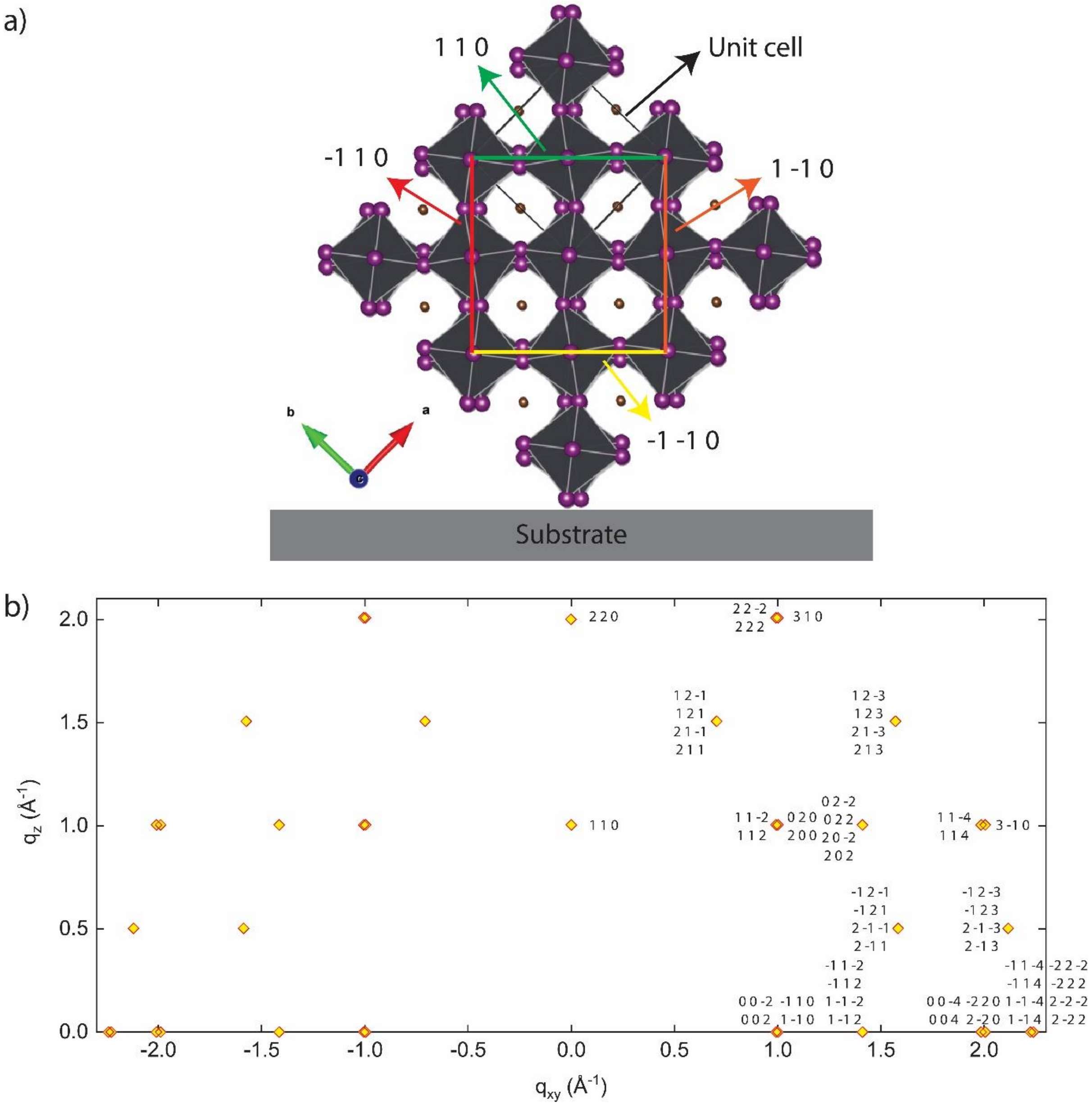

**Figure S7**: (**a**) Schematic illustration of (110) symmetry-equivalent reflections of the textured tetragonal phase of $MAPbI_3$ film with the preferred [110] out-of-plane orientation, and the corresponding (**b**) simulated GIWAXS pattern fully indexed with individual symmetry-equivalent reflections for each peak. The GIWAXS pattern is symmetric about the $q_z$- and $q_{xy}$-axis, however the reflections below $q_z = 0$ Å$^{-1}$ are not shown as the grazing incidence geometry captures only the reflected beam.

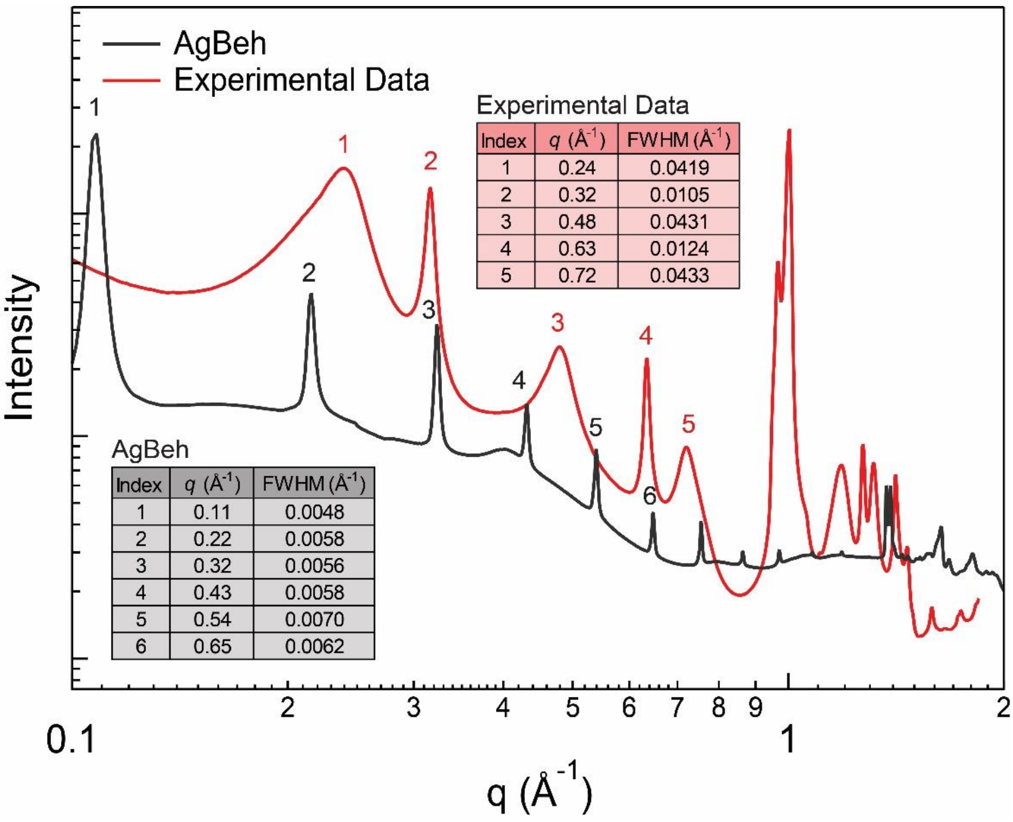

Experimental Data

| Index | $q$ (Å$^{-1}$) | FWHM (Å$^{-1}$) |
|---|---|---|
| 1 | 0.24 | 0.0419 |
| 2 | 0.32 | 0.0105 |
| 3 | 0.48 | 0.0431 |
| 4 | 0.63 | 0.0124 |
| 5 | 0.72 | 0.0433 |

AgBeh

| Index | $q$ (Å$^{-1}$) | FWHM (Å$^{-1}$) |
|---|---|---|
| 1 | 0.11 | 0.0048 |
| 2 | 0.22 | 0.0058 |
| 3 | 0.32 | 0.0056 |
| 4 | 0.43 | 0.0058 |
| 5 | 0.54 | 0.0070 |
| 6 | 0.65 | 0.0062 |

**Figure S8**: Radially integrated TWAXS pattern of silver behenate (AgBeh) calibrant and experimental data (replotted from Figure 3a) plotted on the double logarithmic scale, along with the insets showing the fitted peak positions and FWHMs of labelled peaks. The much larger peak width of experimental data as compared to AgBeh clearly shows that the peak broadening in the experimental data are mostly contributed by the sample-related broadening and the instrumental broadening contribution is insignificant.

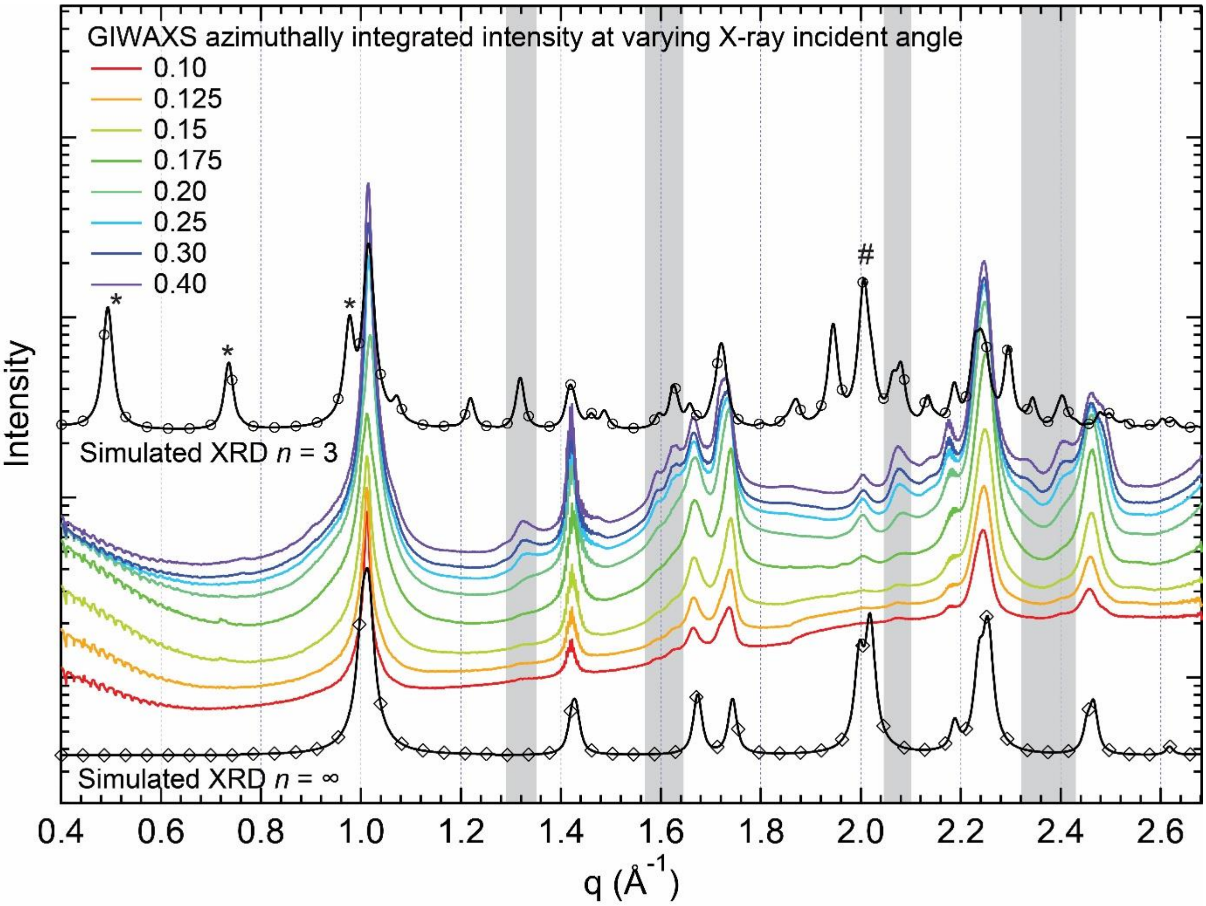

**Figure S9**: Comparison of GIWAXS azimuthally integrated intensities of Ruddlesden-Popper layered perovskite thin film (prepared with target $n = 4$) at varying X-ray incident angle ($\alpha_i$) with the simulated XRD pattern of $n = 3$ and $\infty$ phase. The lower X-ray incident angle probes shallower film microstructure, with the incident angle lower than critical angle (~ 0.15°)[18] probes near-surface microstructure. The GIWAXS patterns collected at lower $\alpha_i$ (eg: $\alpha_i = 0.10°$ and $0.125°$) closely resemble the simulated $n = \infty$ phase XRD pattern whereas the higher $\alpha_i$ GIWAXS patterns (eg: $\alpha_i = 0.30°$ and $0.40°$) match the simulated $n = 3$ phase XRD pattern well as indicated in the shaded grey area, supporting the proposed microstructure that the $n = \infty$ phase is spatially located near the film surface whereas the low-$n$ phases reside near the substrate. The (0$k$0) reflections in the simulated $n = 3$ phase (marked *) is missing in the experimental data as the in-plane scattered X-rays are obscured by the substrate horizon in GIWAXS measurement. The experimental data shows much lower peak intensity at $q \sim 2$ Å$^{-1}$ (marked #) a scompared to simulated XRD patterns because the out-of-plane peaks which fall in the missing wedge are not captured in GIWAXS measurement.

## References

1. F. Huang, Y. Dkhissi, W. Huang, M. Xiao, I. Benesperi, S. Rubanov, Y. Zhu, X. Lin, L. Jiang, Y. Zhou, A. Gray-Weale, J. Etheridge, C. R. McNeill, R. A. Caruso, U. Bach, L. Spiccia and Y.-B. Cheng, *Nano Energy*, 2014, **10**, 10-18.

2. C. Zuo, A. D. Scully, D. Vak, W. Tan, X. Jiao, C. R. McNeill, D. Angmo, L. Ding and M. Gao, *Advanced Energy Materials*, 2019, **9**, 1803258.
3. C. Shi, R. Teerakapibal, L. Yu and G. G. Zhang, *IUCrJ*, 2017, **4**, 555-559.
4. J. Ilavsky, *Journal of Applied Crystallography*, 2012, **45**, 324-328.
5. D. B. Mitzi, *Chemistry of Materials*, 1996, **8**, 791-800.
6. C. C. Stoumpos, D. H. Cao, D. J. Clark, J. Young, J. M. Rondinelli, J. I. Jang, J. T. Hupp and M. G. Kanatzidis, *Chemistry of Materials*, 2016, **28**, 2852-2867.
7. C. C. Stoumpos, C. D. Malliakas and M. G. Kanatzidis, *Inorganic Chemistry*, 2013, **52**, 9019-9038.
8. D.-M. Smilgies and D. R. Blasini, *Journal of Applied Crystallography*, 2007, **40**, 716-718.
9. K. Momma and F. Izumi, *Journal of Applied Crystallography*, 2011, **44**, 1272-1276.
10. N. M. Kirby, S. T. Mudie, A. M. Hawley, D. J. Cookson, H. D. Mertens, N. Cowieson and V. Samardzic-Boban, *Journal of Applied Crystallography*, 2013, **46**, 1670-1680.
11. T. Huang, H. Toraya, T. Blanton and Y. Wu, *Journal of Applied Crystallography*, 1993, **26**, 180-184.
12. G. Williamson and W. Hall, *Acta Metallurgica*, 1953, **1**, 22-31.
13. A. Boulle, C. Legrand, R. Guinebretière, J. Mercurio and A. Dauger, *Journal of Applied Crystallography*, 2001, **34**, 699-703.
14. J. Langford, A. Boultif, J. Auffrédic and D. Louër, *Journal of Applied Crystallography*, 1993, **26**, 22-33.
15. M. S. Paterson, *Journal of Applied Physics*, 1952, **23**, 805-811.
16. A. Boulle, C. Legrand, R. Guinebretiere, J. Mercurio and A. Dauger, *Thin Solid Films*, 2001, **391**, 42-46.
17. C. C. Stoumpos, C. M. M. Soe, H. Tsai, W. Nie, J.-C. Blancon, D. H. Cao, F. Liu, B. Traoré, C. Katan and J. Even, *Chem*, 2017, **2**, 427-440.
18. R. L. Milot, R. J. Sutton, G. E. Eperon, A. A. Haghighirad, J. Martinez Hardigree, L. Miranda, H. J. Snaith, M. B. Johnston and L. M. Herz, *Nano Letters*, 2016, **16**, 7001-7007.